

Asymmetrically filled slits in a metal film that split a light beam into two depending on its wavelength

Danhong Huang¹ and L. David Wellems¹

¹*Air Force Research Laboratory, Space Vehicles Directorate,
Kirtland Air Force Base, NM 87117, USA*

By applying a scattering-wave theory, the electromagnetic response of an arbitrary array of multiple slits perforated on a metallic film and filled with different slit dielectric materials can be studied in an analytical way. Here, the wavelength-dependent splitting of a light beam into two by asymmetrically filled slits in a metal film using intra- and inter-slit dual-wave interferences is fully explored. We consider a triple-slit structure perforated on a gold film, where the middle slit is used for the surface-plasmon excitation by a narrow Gaussian beam while the two side slits are used for the detection of a transmitted surface-plasmon wave propagated from the middle opaque slit either at a particular wavelength or at double that wavelength, respectively. For this proposed simple structure, we show that only one of the two side observation slits can be in a passing state for a particular wavelength, but the other blocked slit will change to a passing state at double that wavelength with a specific design for the slit depth, slit dielectric, and inter-slit distance in the deep sub-wavelength regime. In this sense, surface-plasmon mediated light transmission becomes wavelength sensitive in our model, and a single light beam can be separated into two according to its wavelength in the transverse direction parallel to the array. This provides us with a unique way for direct optical reading in the near-field region using a non-spectroscopic approach.

© 2012 Optical Society of America

OCIS codes:

1. Introduction

Surface-plasmon-polariton modes¹ and localized surface plasmons², which are both localized at an interface between a bulk conductor and a bulk dielectric, have become very hot research subjects in recent years³. The extraordinarily high transmission of a *p*-polarized light beam propagating through a two-dimensional honeycomb lattice of holes on a metal film with sub-wavelength diameters⁴⁻⁶ depends strongly on the lattice constant and the metal-film thickness (also in the deep sub-wavelength regime)^{7,8}.

On the other hand, studies on the surface-plasmon mediated light transmission by a sub-wavelength structure (including random surface roughness) on a designed metal surface have also attracted a lot of attention^{9,10}. For an optically-opaque metal film on a dielectric substrate, if a single slit is perforated on this film, the excited surface plasmons on the front side of the film can be coupled to the backside by intra-slit interferences^{3,11}. In addition, we demonstrate in this paper that not only the intra-slit interference but also the inter-slit interference for a slit array can affect the transmission of the excited surface plasmon propagating through the slits, which was not explored in previous works^{3,11}. The inter-slit interference considered in this paper is related only to the surface wave but not to the surface-plasmon wave, since this interference effect survives even for a perfect electric conductor. It is also important to mention that the surface-plasmon-polariton mode for a planar surface becomes folded with a finite lattice constant in a periodic array and is split into many branches with a minigap opened either at the center or at the edge of the first Brillouin zone¹². Therefore, the surface-plasmon mediated splitting of a light beam studied in this paper has to consider avoiding these minigaps. A related work on plasmonic photon sorters for spectral and polarimetric imaging was reported early¹³, which employed coupled bull-eye structures with a linear modulation in groove depth within each structure.

In our previous study¹⁴, we have shown the longitudinally color-dependent light focusing by a finite linear array of grooves with various widths in a parabolic pattern, where various focal lengths of a slit-array aperture were obtained for an incident plane wave with different colors. Here, rather than using a Green's function formalism^{12,15}, we present a scattering-wave theory which utilizes a slit-eigenmode expansion to treat an arbitrary array of slits having arbitrary spacings, widths and dielectrics. In addition, the derived scattering-wave theory in this paper provides one with a full description to the surface scattering of light by

removing a so-called “diagonal” approximation adopted in a previous related theory^{3,11,16}. Specifically, as an example, in this paper we consider a triple-slit structure in which the middle opaque slit is used for the front-side local surface plasmon excitation by an incident Gaussian beam either at a particular wavelength or at double that wavelength, and the two side slits are used for the wavelength-dependent detection of surface-plasmon mediated light-beam splitting in the near-field region. With our designed narrow-slit depth, slit dielectric, and inter-slit distance, we show that one of the two observation slits can be in a passing state while the other one, at the same time, is in a blocking state for a particular wavelength. Moreover, at double that wavelength, the previously-blocked observation slit switches to a passing state. Therefore, surface-plasmon mediated light-beam splitting becomes wavelength sensitive in our model, and can be spatially separated in the transverse direction parallel to the array. As a result, it provides us with a unique way for direct color reading in the near-field region based on a non-spectroscopic technique. In this paper, we have only cited the most relevant and the most recent advances in the fields of light scattering and surface plasmons, including works reported by us and other groups. The readers who are interested in details of this field are referred to the review article by Garcia-Vidal, *et al.*³

The rest of the paper is organized as follows. In Sec.2, we derive the scattering-wave theory for a non-perfect electric conductor to include the loss of a metallic film in the optical-frequency range by employing a surface impedance boundary condition. This theory is then applied to study the transmission of an electromagnetic field through an arbitrary array of slits perforated on the metallic film and filled with various dielectric materials. The issue about using the surface impedance boundary condition for a film was extensively discussed in Ref.¹⁷. In general, the surface impedance boundary condition can be expressed as a linear relation using a (2×2) impedance matrix and takes a nonlocal or an integral form. The zeroth-order term of the impedance matrix is a local matrix. If the skin depth of a metal film is much smaller than its thickness, which is the situation to be considered in this paper, the off-diagonal elements of the local impedance matrix, which couple two surfaces of a metal film, can be neglected. In Sec.3, numerical results are presented to demonstrate both the passing and blocking states of two observation slits at a particular wavelength and at double that wavelength, along with detailed explanations of these two complementary states based on the intra-slit and inter-slit dual-wave interferences. The conclusions drawn from these results are briefly summarized in Sec.4.

2. Scattering-Wave Theory

A. Basic Formalism

In this paper, we consider only p polarization for an electromagnetic (EM) field, written as $\mathbf{H} = (0, H_y, 0)$, so that the surface-plasmon (SP) wave on a metal-air interface can be excited. Here, the \mathbf{H} field is assumed translationally invariant in the y direction for the array of slits, shown in Fig. 1. We further denote the scalar magnetic-field amplitude as $u(x, z) = H_y(x, z)$. The corresponding electric field can be calculated from $\mathbf{E} = i/(\omega\epsilon_0\epsilon_s) \nabla \times \mathbf{H}$, where ω is the angular frequency and ϵ_s (real) represents the relative dielectric constants of the host materials on the left- ($s = L$) and right-hand ($s = R$) side of a metal film. Since the metal film, which contains a finite slit array, will be treated as a non-perfect electric conductor (non-PEC), we need to employ the so-called surface impedance boundary condition^{18–20} (SIBC) for the total EM field. In our current model, the SIBC requires $\partial u(x, z)/\partial x = \eta_s u(x, z)$ on a metal surface, where $\eta_s = \pm k_0 \epsilon_s / [i\sqrt{-\epsilon_M(\omega)}]$, $k_0 = \omega/c$ is the wave number of the EM field in vacuum, $\epsilon_M(\omega)$ (complex with optical loss) is the metal-film dielectric function, and the \pm signs refer to the left (minus) and right (positive) surfaces of the metal film shown in Fig. 1. The frequency-dependent dielectric function $\epsilon_M(\omega)$ for the gold film is obtained by interpolation from the data in the paper by Johnson and Christy²¹.

By applying the SIBC on the left-hand side (L) of the slit array ($x < -d$), we get

$$\left. \frac{\partial u(x, z)}{\partial x} \right|_{x=-d-0} = \begin{cases} \eta_L u(x, z)|_{x=-d-0} & \text{left surface } z_j + \ell_j < z < z_{j+1} - \ell_{j+1} \\ \frac{\epsilon_L}{\kappa_j} \frac{\partial u(x, z)}{\partial x} \Big|_{x=-d+0} & \text{middle slit } |z - z_j| < \ell_j \\ \eta_L u(x, z)|_{x=-d-0} & \text{right surface } z_{j-1} + \ell_{j-1} < z < z_j - \ell_j \end{cases}, \quad (1)$$

where $2d$ is the thickness of the metal film, $j = 0, \pm 1, \pm 2, \dots, \pm N$ is the slit index, z_j and $2\ell_j$ are the center position and the width of the j th slit, and κ_j (real or complex) is the dielectric constant of the material inside the j th slit. Similarly, after applying the SIBC to the right-hand side (R) of the slit array ($x > d$), we acquire

$$\left. \frac{\partial u(x, z)}{\partial x} \right|_{x=d+0} = \begin{cases} \eta_R u(x, z)|_{x=d+0} & \text{left surface } z_j + \ell_j < z < z_{j+1} - \ell_{j+1} \\ \frac{\epsilon_R}{\kappa_j} \frac{\partial u(x, z)}{\partial x} \Big|_{x=d-0} & \text{middle slit } |z - z_j| < \ell_j \\ \eta_R u(x, z)|_{x=d+0} & \text{right surface } z_{j-1} + \ell_{j-1} < z < z_j - \ell_j \end{cases}. \quad (2)$$

If we set $\eta_L = \eta_R = 0$ in Eqs. (1) and (2), we will simply get the corresponding boundary conditions for a PEC²². In addition, the continuity of $u(x, z)$ is needed for each slit entry: i.e., $u(x, z)|_{x=-d-0} = u(x, z)|_{x=-d+0}$ and $u(x, z)|_{x=d-0} = u(x, z)|_{x=d+0}$. For Lamellar metallic gratings, the PEC boundary condition for the slit side walls was used in calculations of plasmon-mediated light reflection, and the results agreed very well with experimental results^{23,24}. Therefore, for the PEC the field normal derivative must be zero along the slit side walls, i.e.,

$$\left. \frac{\partial u(x, z)}{\partial z} \right|_{z=z_j \pm \ell_j} = 0 \quad \text{for all slits } |x| \leq d. \quad (3)$$

In Region I (the left-hand side of the slit array), the total field, including both the incident and reflected ones, can be written as²²

$$\begin{aligned} u^{(I)}(x, z) = & k_0 \epsilon_L \int_0^\infty \frac{d\beta}{k_1(\beta)} [G_s(\beta) \cos(\beta z) + i G_a(\beta) \sin(\beta z)] e^{ik_1(\beta)(x+d)} \\ & - k_0 \epsilon_L \int_0^\infty \frac{d\beta}{k_1(\beta)} [A_s(\beta) \cos(\beta z) + i A_a(\beta) \sin(\beta z)] e^{-ik_1(\beta)(x+d)}, \end{aligned} \quad (4)$$

where $G_s(\beta)$ and $G_a(\beta)$ are the symmetric and anti-symmetric spectral components of an incident Gaussian beam, given by

$$\begin{aligned} G_s(\beta) &= [G_n(\beta) + G_p(\beta)] \cos(\beta z_G) - i [G_n(\beta) - G_p(\beta)] \sin(\beta z_G), \\ G_a(\beta) &= [G_n(\beta) - G_p(\beta)] \cos(\beta z_G) - i [G_n(\beta) + G_p(\beta)] \sin(\beta z_G), \end{aligned} \quad (5)$$

z_G denotes the Gaussian beam center position, and $G_p(\beta)$ and $G_n(\beta)$ in Eq. (5) are defined as

$$\begin{aligned} G_p(\beta) &= \frac{g k_1(\beta)}{2\sqrt{\pi} \epsilon_L k_0} \exp \left[-\frac{g^2(\beta + \beta_0)^2}{4} \right] \Theta(n_L k_0 - |\beta|), \\ G_n(\beta) &= \frac{g k_1(\beta)}{2\sqrt{\pi} \epsilon_L k_0} \exp \left[-\frac{g^2(\beta - \beta_0)^2}{4} \right] \Theta(n_L k_0 - |\beta|). \end{aligned} \quad (6)$$

In Eq. (6), $\Theta(\beta)$ is the unit step function, $\beta_0 = n_L k_0 \sin \theta_0$, θ_0 is the incident angle of the beam, $n_L = \sqrt{\epsilon_L}$, and $k_1(\beta) = \sqrt{n_L^2 k_0^2 - \beta^2}$ can be either real or complex with $\text{Im}[k_1(\beta)] \geq 0$.

In a similar way, we find that in Region III (the right-hand side of the slit array) the transmitted field takes the form²²

$$u^{(\text{III})}(x, z) = k_0 \epsilon_R \int_0^\infty \frac{d\beta}{k_2(\beta)} [B_s(\beta) \cos(\beta z) + i B_a(\beta) \sin(\beta z)] e^{i k_2(\beta)(x-d)}, \quad (7)$$

where $n_R = \sqrt{\epsilon_R}$ and $k_2(\beta) = \sqrt{n_R^2 k_0^2 - \beta^2}$ with $\text{Im}[k_2(\beta)] \geq 0$.

Finally, in Region II (middle slit array), using the eigenmode expansion [subjected to the boundary condition in Eq. (3)], we obtain²²

$$u^{(\text{II})}(x, z) = k_0 \sum_j \Theta(\ell_j - |z - z_j|) \sum_n \left\{ \frac{\kappa_j}{\sigma_{sn}^j} \left[a_{sn}^j e^{i\sigma_{sn}^j(x+d)} - b_{sn}^j e^{-i\sigma_{sn}^j(x-d)} \right] \right. \\ \left. \times \cos[\xi_{sn}^j(z - z_j)] + i \frac{\kappa_j}{\sigma_{an}^j} \left[a_{an}^j e^{i\sigma_{an}^j(x+d)} - b_{an}^j e^{-i\sigma_{an}^j(x-d)} \right] \sin[\xi_{an}^j(z - z_j)] \right\}, \quad (8)$$

where $n = 1, 2, \dots$ is the eigenmode index, $\xi_{sn}^j = (\pi/\ell_j)(n - 1)$ and $\xi_{an}^j = (\pi/\ell_j)(n - 1/2)$ are for symmetric and anti-symmetric slit eigenmodes, respectively, and $\sigma_{sn,an}^j = \sqrt{\kappa_j k_0^2 - (\xi_{sn,an}^j)^2}$ can be either real or complex, with $\text{Re}[\sigma_{sn,an}^j] \geq 0$.

When $n = 0$, the lowest symmetric eigenmode in Eq. (8) corresponds to a uniform EM field distribution in the z direction within each slit. The evanescent waves can exist only when $k_1(\beta)$ or $k_2(\beta)$ is purely imaginary, i.e., $\beta > n_L k_0$ for the reflection side or $\beta > n_R k_0$ for the transmission side. On the other hand, the condition for a pure scattered surface wave is obtained through $k_1(\beta) \rightarrow 0$ or $k_2(\beta) \rightarrow 0$. This condition can be met by $\beta = n_L k_0$ for reflection or $\beta = n_R k_0$ for transmission.

B. SIBC Constraints

By using the derivative boundary conditions in Eqs. (1) and (2) at $x = \pm d$ and the orthogonality of the continuous Fourier expansions in Eqs. (4) and (7), a set of constraint equations for the unknown Fourier coefficients $A_s(\beta)$, $A_a(\beta)$, $B_s(\beta)$ and $B_a(\beta)$ can be obtained.

At $x = -d$, from Eq. (1) we get

$$\begin{aligned}
& \int_0^\infty d\beta \{ [G_s(\beta) + A_s(\beta)] \cos(\beta z) + i [G_a(\beta) + A_a(\beta)] \sin(\beta z) \} \\
&= -i\eta_L \epsilon_L \int_0^\infty \frac{d\beta}{k_1(\beta)} \{ [G_s(\beta) - A_s(\beta)] \cos(\beta z) + i [G_a(\beta) - A_a(\beta)] \sin(\beta z) \} \quad (9)
\end{aligned}$$

for z values within the non-slit regions of a non-PEC, and

$$\begin{aligned}
& \int_0^\infty d\beta \{ [G_s(\beta) + A_s(\beta)] \cos(\beta z) + i [G_a(\beta) + A_a(\beta)] \sin(\beta z) \} \\
&= \sum_j \Theta(\ell_j - |z - z_j|) \sum_n \left[\left(a_{sn}^j + b_{sn}^j e^{i\sigma_{sn}^j 2d} \right) \cos[\xi_{sn}^j(z - z_j)] \right. \\
& \quad \left. + i \left(a_{an}^j + b_{an}^j e^{i\sigma_{an}^j 2d} \right) \sin[\xi_{an}^j(z - z_j)] \right] \quad (10)
\end{aligned}$$

for the slit regions. Similarly, at $x = d$ we find from Eq. (2)

$$\begin{aligned}
& \int_0^\infty d\beta [B_s(\beta) \cos(\beta z) + i B_a(\beta) \sin(\beta z)] \\
&= -i\eta_R \epsilon_R \int_0^\infty \frac{d\beta}{k_2(\beta)} [B_s(\beta) \cos(\beta z) + i B_a(\beta) \sin(\beta z)] \quad (11)
\end{aligned}$$

for z values within the non-slit regions, and

$$\begin{aligned}
& \int_0^\infty d\beta [B_s(\beta) \cos(\beta z) + i B_a(\beta) \sin(\beta z)] = \sum_j \Theta(\ell_j - |z - z_j|) \sum_n \left[\left(b_{sn}^j \right. \right. \\
& \quad \left. \left. + a_{sn}^j e^{i\sigma_{sn}^j 2d} \right) \cos[\xi_{sn}^j(z - z_j)] + i \left(b_{an}^j + a_{an}^j e^{i\sigma_{an}^j 2d} \right) \sin[\xi_{an}^j(z - z_j)] \right] \quad (12)
\end{aligned}$$

for the slit regions.

C. Projection of SIBC

Since the combination of Eqs. (9) and (10) extends over the left surface of a metal film, we can project out the symmetric and anti-symmetric Fourier coefficients in $u^{(1)}(x, z)$ through multiplying these two equations by $\cos(\beta' z)$ or $\sin(\beta' z)$ and integrating over z afterwards. This leads to

$$\begin{aligned}
A_s(\beta) + G_s(\beta) &= \sum_n \left\{ \sum_j \frac{\ell_j}{\pi} \left[\left(a_{sn}^j + b_{sn}^j e^{2i\sigma_{sn}^j d} \right) Q_{sn}^j(\beta) \cos(\beta z_j) \right. \right. \\
&- i \left(a_{an}^j + b_{an}^j e^{2i\sigma_{an}^j d} \right) Q_{an}^j(\beta) \sin(\beta z_j) \left. \right] \Big\} \\
&- i\eta_L \int_0^\infty \frac{d\beta'}{k_1(\beta')} [P_s(\beta, \beta') + W_s(\beta, \beta')] [G_s(\beta') - A_s(\beta')] \\
&+ \eta_L \int_0^\infty \frac{d\beta'}{k_1(\beta')} [P_c(\beta, \beta') + W_c(\beta, \beta')] [G_a(\beta') - A_a(\beta')] , \tag{13}
\end{aligned}$$

$$\begin{aligned}
A_a(\beta) + G_a(\beta) &= \sum_n \left\{ \sum_j \frac{\ell_j}{\pi} \left[-i \left(a_{sn}^j + b_{sn}^j e^{2i\sigma_{sn}^j d} \right) Q_{sn}^j(\beta) \sin(\beta z_j) \right. \right. \\
&+ \left(a_{an}^j + b_{an}^j e^{2i\sigma_{an}^j d} \right) Q_{an}^j(\beta) \cos(\beta z_j) \left. \right] \Big\} \\
&- \eta_L \int_0^\infty \frac{d\beta'}{k_1(\beta')} [P_c(\beta', \beta) + W_c(\beta', \beta)] [G_s(\beta') - A_s(\beta')] \\
&- i\eta_L \int_0^\infty \frac{d\beta'}{k_1(\beta')} [P_a(\beta, \beta') + W_a(\beta, \beta')] [G_a(\beta') - A_a(\beta')] , \tag{14}
\end{aligned}$$

where the definitions of $Q_{sn}^j(\beta)$ and $Q_{an}^j(\beta)$ can be found from Appendix A.

For the same reason, using Eqs. (11) and (12) we can also project out the symmetric and anti-symmetric Fourier coefficients in $u^{(\text{III})}(x, z)$ through multiplying them by $\cos(\beta'z)$ or $\sin(\beta'z)$ and doing a follow-up z integration. This yields

$$\begin{aligned}
B_s(\beta) &= \sum_n \left\{ \sum_j \frac{\ell_j}{\pi} \left[\left(b_{sn}^j + a_{sn}^j e^{2i\sigma_{sn}^j d} \right) Q_{sn}^j(\beta) \cos(\beta z_j) \right. \right. \\
&- i \left(b_{an}^j + a_{an}^j e^{2i\sigma_{an}^j d} \right) Q_{an}^j(\beta) \sin(\beta z_j) \left. \right] \Big\} \\
&- i\eta_R \int_0^\infty \frac{d\beta'}{k_2(\beta')} [P_s(\beta, \beta') + W_s(\beta, \beta')] B_s(\beta') \\
&+ \eta_R \int_0^\infty \frac{d\beta'}{k_2(\beta')} [P_c(\beta, \beta') + W_c(\beta, \beta')] B_a(\beta') , \tag{15}
\end{aligned}$$

$$\begin{aligned}
B_a(\beta) = & \sum_n \left\{ \sum_j \frac{\ell_j}{\pi} \left[-i \left(a_{sn}^j + b_{sn}^j e^{2i\sigma_{sn}^j d} \right) Q_{sn}^j(\beta) \sin(\beta z_j) \right. \right. \\
& + \left. \left(a_{an}^j + b_{an}^j e^{2i\sigma_{an}^j d} \right) Q_{an}^j(\beta) \cos(\beta z_j) \right] \Big\} \\
& - \eta_R \int_0^\infty \frac{d\beta'}{k_2(\beta')} [P_c(\beta', \beta) + W_c(\beta', \beta)] B_s(\beta') \\
& - i\eta_R \int_0^\infty \frac{d\beta'}{k_2(\beta')} [P_a(\beta, \beta') + W_a(\beta, \beta')] B_a(\beta') .
\end{aligned} \tag{16}$$

The definition of the coupling matrices $P_s(\beta, \beta')$, $P_a(\beta, \beta')$, $P_c(\beta, \beta')$, $W_s(\beta, \beta')$, $W_a(\beta, \beta')$, and $W_c(\beta, \beta')$ can be found in Appendix B. Without loss of generality, we assume an order for the slit array $-\infty < (z_{-N} - \ell_{-N}) < (z_{-N} + \ell_{-N}) < \dots < (z_{-1} - \ell_{-1}) < (z_{-1} + \ell_{-1}) < (z_0 - \ell_0) < (z_0 + \ell_0) < (z_1 - \ell_1) < (z_1 + \ell_1) < \dots < (z_N - \ell_N) \leq (z_N + \ell_N) < \infty$.

If $\eta_L = \eta_R = 0$ for a PEC, we can explicitly express²² the continuous Fourier expansion coefficients $A_s(\beta)$, $A_a(\beta)$, $B_s(\beta)$ and $B_a(\beta)$ by the discrete Fourier expansion coefficients a_{sn}^j , b_{sn}^j , a_{an}^j and b_{an}^j through Eqs. (13), (14), (15) and (16). If there exists only one slit ($j = 0$ and $z_0 = 0$), the PEC single slit does not couple symmetric modes to anti-symmetric ones²⁵. In addition, we find $W_s(\beta, \beta') = W_a(\beta, \beta') = W_c(\beta, \beta') = 0$ and $P_c(\beta, \beta') = 0$ in this case. Therefore, the non-PEC single slit cannot couple symmetric modes to anti-symmetric ones. For a symmetric distribution of slits with respect to $z_0 = 0$, we always have $|z_{-N} - \ell_{-N}| = z_N + \ell_N$, leading to $P_c(\beta, \beta') = 0$. However, in this multi-slit case, $W_c(\beta, \beta') \neq 0$. As a result, symmetric and anti-symmetric modes are coupled to each other. If we treat the SIBC in Eqs. (13), (14), (15) and (16) as a perturbation for small η_L and η_R , we can express $A_s(\beta)$, $A_a(\beta)$, $B_s(\beta)$ and $B_a(\beta)$ by the discrete Fourier expansion coefficients a_{sn}^j , b_{sn}^j , a_{an}^j and b_{an}^j to the leading order of the perturbation. Alternatively, if only the diagonal contributions for the term proportional to η_L or η_R are kept^{3,11,16} in Eqs. (13), (14), (15) and (16) [i.e., including only the terms with $\beta' = \pm\beta$ in the integrals], $A_s(\beta)$, $A_a(\beta)$, $B_s(\beta)$ and $B_a(\beta)$ can also be expressed by the discrete Fourier expansion coefficients a_{sn}^j , b_{sn}^j , a_{an}^j and b_{an}^j . However, such a simplification^{3,11,16} needs to be justified physically.

The projected SBIC in Eqs. (13)-(16) leads to the approximate field equations derived in References^{3,11,16} after applying the ‘‘diagonal approximation’’ for simplification. It is clear from Eqs. (13)-(16) that such a ‘‘diagonal approximation’’ can only be justified when the

coefficients $P_s(\beta, \beta')$, $P_c(\beta, \beta')$, $P_a(\beta, \beta')$, as well as the coefficients $W_s(\beta, \beta')$, $W_c(\beta, \beta')$, $W_a(\beta, \beta')$, are either peaked around $\beta = \beta'$ or negligibly small. We further realize from Appendices B & C that $P_s(\beta, \beta')$, $P_a(\beta, \beta')$ always peak around $\beta = \beta'$ due to the existence of the $\delta(\beta - \beta')$ terms; $W_s(\beta, \beta')$, $W_a(\beta, \beta')$ can peak around $\beta = \beta'$ only if neighboring slits are well separated from each other in comparison with the inverses of β and β' due to the existence of sinc-function terms; both $P_c(\beta, \beta')$ and $W_c(\beta, \beta')$ can be neglected only for very large β , β' and $\beta \neq \beta'$ due to the existence of cosine terms. Therefore, the advantage of the current theory is its immunization from such restrictions and it can be applied to general cases.

D. Integral Equations

In order to get the closed-form integral equations for a non-PEC, we look to express a_{sn}^j , a_{an}^j , b_{sn}^j and b_{an}^j in Eqs. (13), (14), (15) and (16) by $A_s(\beta)$, $A_a(\beta)$, $B_s(\beta)$ and $B_a(\beta)$. This can be achieved by using the orthogonality of the discrete Fourier expansion in Eq. (8) and multiplying both sides of the continuity conditions for slit entries and exits, i.e. $u^{(I)}(x = -d, z) = u^{(II)}(x = -d, z)$ and $u^{(III)}(x = d, z) = u^{(II)}(x = d, z)$, by $\cos[\xi_{sn'}^{j'}(z - z_{j'})]$ or $\sin[\xi_{an'}^{j'}(z - z_{j'})]$, which is followed by an integration of z over all the slit regions. This yields

$$\begin{aligned} \frac{\chi_n \kappa_j}{\sigma_{sn}^j \epsilon_L} \left(a_{sn}^j - b_{sn}^j e^{2i\sigma_{sn}^j d} \right) &= \int_0^\infty \frac{d\beta}{k_1(\beta)} [G_s(\beta) - A_s(\beta)] Q_{sn}^j(\beta) \cos(\beta z_j) \\ &+ i \int_0^\infty \frac{d\beta}{k_1(\beta)} [G_a(\beta) - A_a(\beta)] Q_{sn}^j(\beta) \sin(\beta z_j), \end{aligned} \quad (17)$$

$$\begin{aligned} \frac{\chi_n \kappa_j}{\sigma_{an}^j \epsilon_L} \left(a_{an}^j - b_{an}^j e^{2i\sigma_{an}^j d} \right) &= i \int_0^\infty \frac{d\beta}{k_1(\beta)} [G_s(\beta) - A_s(\beta)] Q_{an}^j(\beta) \sin(\beta z_j) \\ &+ \int_0^\infty \frac{d\beta}{k_1(\beta)} [G_a(\beta) - A_a(\beta)] Q_{an}^j(\beta) \cos(\beta z_j), \end{aligned} \quad (18)$$

$$\begin{aligned} \frac{\chi_n \kappa_j}{\sigma_{sn}^j \epsilon_R} \left(a_{sn}^j e^{2i\sigma_{sn}^j d} - b_{sn}^j \right) &= \int_0^\infty \frac{d\beta}{k_2(\beta)} B_s(\beta) Q_{sn}^j(\beta) \cos(\beta z_j) \\ &+ i \int_0^\infty \frac{d\beta}{k_2(\beta)} B_a(\beta) Q_{sn}^j(\beta) \sin(\beta z_j), \end{aligned} \quad (19)$$

$$\begin{aligned}
\frac{\chi_n \kappa_j}{\sigma_{an}^j \epsilon_R} \left(a_{an}^j e^{2i\sigma_{an}^j d} - b_{an}^j \right) &= i \int_0^\infty \frac{d\beta}{k_2(\beta)} B_s(\beta) Q_{an}^j(\beta) \sin(\beta z_j) \\
+ \int_0^\infty \frac{d\beta}{k_2(\beta)} B_a(\beta) Q_{an}^j(\beta) \cos(\beta z_j) , & \quad (20)
\end{aligned}$$

where $\chi_n = 2$ for $n = 1$ and $\chi_n = 1$ for $n \neq 1$. Equations (17) and (18) connect the j th-slit field at the entry edge to the total field in Region I, where the forward-moving amplitude, a_{sn}^j or a_{an}^j , and backward-moving amplitude, b_{sn}^j or b_{an}^j , can be viewed as two independent interfering waves with phase delays of $2i\sigma_{sn}^j d$ or $2i\sigma_{an}^j d$. The same arguments can be applied to Eqs. (19) and (20) at the exit edge of the j th slit.

Equations (17) through Eq. (20) can be formally solved analytically, which leads to

$$\begin{aligned}
a_{sn}^j &= \frac{Y_{jn}^{(2)} - e^{-2i\sigma_{sn}^j d} Y_{jn}^{(1)}}{2i \sin(2\sigma_{sn}^j d)} , & b_{sn}^j &= \frac{e^{-2i\sigma_{sn}^j d} Y_{jn}^{(2)} - Y_{jn}^{(1)}}{2i \sin(2\sigma_{sn}^j d)} , \\
a_{an}^j &= \frac{X_{jn}^{(2)} - e^{-2i\sigma_{an}^j d} X_{jn}^{(1)}}{2i \sin(2\sigma_{an}^j d)} , & b_{an}^j &= \frac{e^{-2i\sigma_{an}^j d} X_{jn}^{(2)} - X_{jn}^{(1)}}{2i \sin(2\sigma_{an}^j d)} . & (21)
\end{aligned}$$

Here, a_{sn}^j and a_{an}^j represents the forward-moving waves, while b_{sn}^j and b_{an}^j represents the backward-moving waves. Whenever $2\sigma_{sn}^j d/\pi$ or $2\sigma_{an}^j d/\pi$ becomes an integer, the constructive or destructive dual-wave interference will occur at two the edges of the j th slit for the n th eigenmode. In this case, the slit behaves either like a passing filter or like a cavity for field trapping. The definitions of $Y_{jn}^{(1)}$, $Y_{jn}^{(2)}$, $X_{jn}^{(1)}$, and $X_{jn}^{(2)}$ introduced in Eq. (21) can be found in Appendix C. Here, $X_{jn}^{(1)}$ and $Y_{jn}^{(1)}$ come from the contribution of $u^{(I)}(x, z)$ at the left slit entry, while $X_{jn}^{(2)}$ and $Y_{jn}^{(2)}$ come from the contribution of $u^{(III)}(x, z)$ at the right slit exit. For a PEC, by substituting Eqs. (13), (14), (15) and (16) with $\eta_L = \eta_R = 0$ into Eqs. (17)–(20), we get a set of inhomogeneous linear equations²² with respect to a_{sn}^j , b_{sn}^j , a_{an}^j and b_{an}^j .

Using the results in Eq. (21), from Eqs. (13), (14), (15) and (16) we finally obtain four integral equations for $A_s(\beta)$, $A_a(\beta)$, $B_s(\beta)$ and $B_a(\beta)$

$$\begin{aligned}
G_s(\beta) + A_s(\beta) = & -i\eta_L \int_0^\infty \frac{d\beta'}{k_1(\beta')} [P_s(\beta, \beta') + W_s(\beta, \beta')] [G_s(\beta') - A_s(\beta')] \\
& + \eta_L \int_0^\infty \frac{d\beta'}{k_1(\beta')} [P_c(\beta, \beta') + W_c(\beta, \beta')] [G_a(\beta') - A_a(\beta')] \\
& + \int_0^\infty \frac{d\beta'}{k_2(\beta')} [T_s^{(1)}(\beta, \beta') B_s(\beta') + iT_s^{(2)}(\beta, \beta') B_a(\beta')] \\
& - \int_0^\infty \frac{d\beta'}{k_1(\beta')} \{T_s^{(3)}(\beta, \beta') [G_s(\beta') - A_s(\beta')] + iT_s^{(4)}(\beta, \beta') [G_a(\beta') - A_a(\beta')]\} \\
& - i \int_0^\infty \frac{d\beta'}{k_2(\beta')} [R_s^{(1)}(\beta, \beta') B_a(\beta') + iR_s^{(2)}(\beta, \beta') B_s(\beta')] \\
& + i \int_0^\infty \frac{d\beta'}{k_1(\beta')} \{R_s^{(3)}(\beta, \beta') [G_a(\beta') - A_a(\beta')] \\
& + iR_s^{(4)}(\beta, \beta') [G_s(\beta') - A_s(\beta')]\} , \tag{22}
\end{aligned}$$

$$\begin{aligned}
G_a(\beta) + A_a(\beta) = & -\eta_L \int_0^\infty \frac{d\beta'}{k_1(\beta')} [P_c(\beta', \beta) + W_c(\beta', \beta)] [G_s(\beta') - A_s(\beta')] \\
& - i\eta_L \int_0^\infty \frac{d\beta'}{k_1(\beta')} [P_a(\beta, \beta') + W_a(\beta, \beta')] [G_a(\beta') - A_a(\beta')] \\
& - i \int_0^\infty \frac{d\beta'}{k_2(\beta')} [T_a^{(1)}(\beta, \beta') B_s(\beta') + iT_a^{(2)}(\beta, \beta') B_a(\beta')] \\
& + i \int_0^\infty \frac{d\beta'}{k_1(\beta')} \{T_a^{(3)}(\beta, \beta') [G_s(\beta') - A_s(\beta')] + iT_a^{(4)}(\beta, \beta') [G_a(\beta') - A_a(\beta')]\} \\
& + \int_0^\infty \frac{d\beta'}{k_2(\beta')} [R_a^{(1)}(\beta, \beta') B_a(\beta') + iR_a^{(2)}(\beta, \beta') B_s(\beta')] \\
& - \int_0^\infty \frac{d\beta'}{k_1(\beta')} \{R_a^{(3)}(\beta, \beta') [G_a(\beta') - A_a(\beta')] \\
& + iR_a^{(4)}(\beta, \beta') [G_s(\beta') - A_s(\beta')]\} , \tag{23}
\end{aligned}$$

$$\begin{aligned}
B_s(\beta) = & -i\eta_R \int_0^\infty \frac{d\beta'}{k_2(\beta')} [P_s(\beta, \beta') + W_s(\beta, \beta')] B_s(\beta') \\
& + \eta_R \int_0^\infty \frac{d\beta'}{k_2(\beta')} [P_c(\beta, \beta') + W_c(\beta, \beta')] B_a(\beta') \\
& + \int_0^\infty \frac{d\beta'}{k_2(\beta')} [N_s^{(1)}(\beta, \beta') B_s(\beta') + iN_s^{(2)}(\beta, \beta') B_a(\beta')] \\
& - \int_0^\infty \frac{d\beta'}{k_1(\beta')} \{N_s^{(3)}(\beta, \beta') [G_s(\beta') - A_s(\beta')] + iN_s^{(4)}(\beta, \beta') [G_a(\beta') - A_a(\beta')]\} \\
& - i \int_0^\infty \frac{d\beta'}{k_2(\beta')} [M_s^{(1)}(\beta, \beta') B_a(\beta') + iM_s^{(2)}(\beta, \beta') B_s(\beta')] \\
& + i \int_0^\infty \frac{d\beta'}{k_1(\beta')} \{M_s^{(3)}(\beta, \beta') [G_a(\beta') - A_a(\beta')] \\
& + iM_s^{(4)}(\beta, \beta') [G_s(\beta') - A_s(\beta')]\} , \tag{24}
\end{aligned}$$

$$\begin{aligned}
B_a(\beta) = & -\eta_R \int_0^\infty \frac{d\beta'}{k_2(\beta')} [P_c(\beta', \beta) + W_c(\beta', \beta)] B_s(\beta') \\
& - i\eta_R \int_0^\infty \frac{d\beta'}{k_2(\beta')} [P_a(\beta, \beta') + W_a(\beta, \beta')] B_a(\beta') \\
& - i \int_0^\infty \frac{d\beta'}{k_2(\beta')} [N_a^{(1)}(\beta, \beta') B_s(\beta') + iN_a^{(2)}(\beta, \beta') B_a(\beta')] \\
& + i \int_0^\infty \frac{d\beta'}{k_1(\beta')} \{N_a^{(3)}(\beta, \beta') [G_s(\beta') - A_s(\beta')] + iN_a^{(4)}(\beta, \beta') [G_a(\beta') - A_a(\beta')]\} \\
& + \int_0^\infty \frac{d\beta'}{k_2(\beta')} [M_a^{(1)}(\beta, \beta') B_a(\beta') + iM_a^{(2)}(\beta, \beta') B_s(\beta')] \\
& - \int_0^\infty \frac{d\beta'}{k_1(\beta')} \{M_a^{(3)}(\beta, \beta') [G_a(\beta') - A_a(\beta')] \\
& + iM_a^{(4)}(\beta, \beta') [G_s(\beta') - A_s(\beta')]\} . \tag{25}
\end{aligned}$$

The expressions for the matrices $T_s^{(\alpha)}(\beta, \beta')$, $R_s^{(\alpha)}(\beta, \beta')$, $M_s^{(\alpha)}(\beta, \beta')$ and $N_s^{(\alpha)}(\beta, \beta')$, as well

as for $T_a^{(\alpha)}(\beta, \beta')$, $R_a^{(\alpha)}(\beta, \beta')$, $M_a^{(\alpha)}(\beta, \beta')$ and $N_a^{(\alpha)}(\beta, \beta')$, with $\alpha = 1, 2, 3, 4$ are given explicitly in Appendix D. In general, $T_{s,a}^{(1,2)}(\beta, \beta')$, $R_{s,a}^{(1,2)}(\beta, \beta')$, $M_{s,a}^{(1,2)}(\beta, \beta')$ and $N_{s,a}^{(1,2)}(\beta, \beta')$ come from the contribution of $u^{(\text{III})}(x, z)$, while $T_{s,a}^{(3,4)}(\beta, \beta')$, $R_{s,a}^{(3,4)}(\beta, \beta')$, $M_{s,a}^{(3,4)}(\beta, \beta')$ and $N_{s,a}^{(3,4)}(\beta, \beta')$ come from the contribution of $u^{(\text{I})}(x, z)$. If the array is infinite and all the slits, as well as the filled dielectric materials, are identical for a periodic system,^{19,20,26,27} the continuous variable β becomes a discrete reciprocal wave number $j(2\pi/\mathcal{D})$ where \mathcal{D} is the array period and $j = 0, \pm 1, \dots$.

There are three different interferences discussed in this paper, namely, intra-slit and inter-slit dual-wave interferences and Fabry-Pérot sole-wave interference. First, for the intra-slit dual-wave interference, we consider the interference between the forward and backward moving slit waves. For the backward moving wave, there already exists a π phase delay and the latter interferes with the former after its reflection from the entrance side of a slit. Therefore, the constructive interference condition (on-state) between these two waves is simply given by $\sqrt{\kappa} k_0 4d = (2m - 1)\pi$, where k_0 is the wave number in vacuum, κ is the slit dielectric constant and $m = \pm 1, \pm 2, \dots$ is an integer. For the same reason, the destructive interference condition (off-state) is given by $\sqrt{\kappa} k_0 4d = 2m\pi$. Second, by the inter-slit dual-wave interference we mean the interference between a backward moving reflected slit wave and a surface wave propagated from another slit and entering forward into the side slit studied. In comparison with the intra-slit dual-wave interference, there exists an additional phase compensation for the forward moving slit wave in this case, which depends only on the slit separation for the surface wave but not on the metal dielectric function. Therefore, we expect a strong influence from the inter-slit dual-wave interference on the intra-slit dual-wave interference. At last, for the Fabry-Pérot sole-wave interference, on the other hand, it is the interference between a forward moving slit wave and the same wave after it has been reflected twice successively by the exit and entrance sides of a slit. Therefore, the constructive Fabry-Pérot interference condition takes the form of $\sqrt{\kappa} k_0 4d = 2m\pi$, which sits at the same position as that of the destructive intra-slit dual-wave interference, and its strength goes up with increased finesse in a longer slit.

3. Numerical Results and Discussions

In this paper, we would like to demonstrate a direct optical reading of fundamental and second-harmonic near-field photon emissions in the near-field region using a non-

spectroscopic technique with specifically designed slit depth, slit dielectric material, and inter-slit distance. In our calculations, we take $\epsilon_L = 1$ (air) and $\epsilon_R = 20, 25$ (high-dielectric-constant oxides). For a triple-slit structure, we illuminate the middle slit and find conditions under which one of the side slits is in a passing state for a particular wavelength (with the other slit in a blocking state) while the other side slit is in a passing state for twice that wavelength (with the other slit again in a blocking state). Here, the passing state of a slit refers to the fact that a surface wave propagated from the middle slit can pass through a vertical slit to get to Region III from Region I, while the blocking state corresponds to a surface wave not passing through a slit due to interference effects. From Eqs. (17)–(20) we find that the forward and backward moving waves inside a slit can be treated as two independent waves, which are decided by the fields in Regions I and III, respectively. As a result, the intra-slit interference in this paper can be viewed as a dual-wave interference, which is quite different from the geometric series result of a typical Fabry-Pérot (FP) slit model. FP cavity analysis utilizes intra-slit reflection and transmission coefficients for a single wave which are not related to the total field structures at the slit edges. It is also important to know that there is already an extra π -phase shift in Eq. (8) due to opposite signs for the forward-moving wave (+) and the backward-moving wave (−). Therefore, for a given incident wavelength λ_0 in vacuum, the constructive intra-slit dual-wave interference, or the passing state of a slit, is found to satisfy the condition: $4d = (2m - 1)\lambda_0/2\sqrt{\kappa}$ with $m = 0, \pm 1, \pm 2, \dots$, where κ is the slit dielectric constant. Moreover, the condition for the destructive intra-slit dual-wave interference, or the blocking state of a slit, is given by $4d = 2m\lambda_0/2\sqrt{\kappa}$ with $m = \pm 1, \pm 2, \dots$. Whether for plane wave or SPP excitation of a single slit, the constructive or destructive dual-wave interference results agree with the zero-order transmission coefficient in a single-mode approximation³. The above interference conditions are not directly derived from the theory described in Sec. 2. However, these phenomenological arguments are found to explain the numerical results in this paper pretty well.

By employing the mechanism for the intra-slit dual-wave interference discussed above, Fig. 2 simultaneously displays the passing state of the left slit as well as the blocking state of the right slit at $\lambda_0 = 0.588 \mu\text{m}$, where the middle slit is used for a local front-side SP excitation, as seen from Eq. (6), and is filled with a wide-band attenuator to prevent light from leaking into Region III. When the slit depth $2d$ becomes larger than λ_0 and the slit

width $2\ell_j$ is only half of λ_0 , all the slit modes for p polarization become strongly attenuated except for the lowest symmetric one which has a uniform distribution in the transverse (z) direction of a slit. For this lowest symmetric mode, the dual-wave constructive-interference condition for the left-slit is satisfied due to $4d = 7\lambda_0/2\sqrt{\kappa_{-1}}$ and $\sqrt{\kappa_{-1}} = 1$. We further find that the dual-wave destructive-interference condition for the right-slit is met at the same time due to $4d = 14\lambda_0/2\sqrt{\kappa_1}$ and $\sqrt{\kappa_1} = 2$. This fully explains the observed left-slit passing state as well as the right-slit blocking state in Fig. 2.

In order to get a complete picture about the intra-slit dual-wave interference after the propagation of an SP wave locally excited at the middle slit, we present in Fig. 3 the averaged ratio of $|H_y(x, z)|^2$ over a slit at $\lambda_0 = 0.588 \mu\text{m}$ as a function of slit depth d for two observation slits at a distance δ slightly away from the backside ($z = d$) of the metal film. For the left slit at $z = z_{-1}$ (blue solid curve), we find from Fig. 3 that there exist four minima at $d/\lambda_0 = 2/8, 4/8, 6/8$ and $8/8$, which agree with the dual-wave destructive-interference condition, i.e., $4d = 2m\lambda_0/2\sqrt{\kappa_{-1}}$ with $m = 1, 2, 3, 4$ and $\sqrt{\kappa_{-1}} = 1$. Similarly, for the right slit at $z = z_1$ (red dashed curve), we find eight minima at $d/\lambda_0 = 2/16, 4/16, \dots, 14/16$ and $16/16$, which also agree with the right-slit dual-wave destructive-interference condition, i.e., $4d = 2m\lambda_0/2\sqrt{\kappa_1}$ with $m = 1, 2, \dots, 7, 8$ and $\sqrt{\kappa_1} = 2$. In addition, a maximum is always seen between two adjacent minima for the right slit, which meets the dual-wave constructive-interference relation, i.e., $4d = (2m - 1)\lambda_0/2\sqrt{\kappa_1}$ with $m = 1, 2, \dots, 7, 8$. However, for the left slit, instead of four maxima as expected, we only see four dips at $d/\lambda_0 = 1/8, 3/8, 5/8$ and $7/8$ due to the effect of an inter-slit dual-wave interference explained below. We note that the slit widths in Figs. 2 and 3 are different, but it will not change the peak and valley positions for the dominant lowest symmetric slit mode.

It is important to mention that the inter-slit distance in Fig. 3 is set to be $(z_1 - z_{-1})/\lambda_0 = 3.75$, which is a quarter wavelength smaller than a multiple of the wavelength λ_0 . In order to understand the inter-slit dual-wave interference effect, we show in Fig. 4 the slit-averaged ratio of $|H_y(x, z)|^2$ at $\lambda_0 = 0.588 \mu\text{m}$ as a function of d for $z_{-1} = -1.5\lambda_0$ in Fig. 4(a) and $z_{-1} = -2\lambda_0$ in Fig. 4(b) with $z_1 = 2\lambda_0$ fixed. When $d/\lambda_0 = 1/8, 3/8, 5/8$ and $7/8$, from Fig. 3 we already know that the contributions from the exit-edge reflected forward-moving waves are out of phase at the left and right slits since the former is in a passing state while the latter is in a blocking state. Therefore, for the case with $(z_1 - z_{-1})/\lambda_0 = 3.5$ in Fig. 4(a),

we expect a constructive inter-slit dual-wave interference to occur at the left slit (blue solid curve), which can be verified by noticing the change of a dip in Fig. 3 into a maximum in Fig. 4(a). However, when $(z_1 - z_{-1})/\lambda_0 = 4$ as shown in Fig. 4(b), the dip in Fig. 3 changes into a full minimum (blue solid curve) as a consequence of the destructive inter-slit dual-wave interference.

As a complementary result to the left-slit passing state at a particular wavelength $\lambda_0 = 0.58 \mu\text{m}$ in Fig. 2, we present another contour plot for the EM field distribution at double that wavelength $\lambda_0 = 1.176 \mu\text{m}$ in Fig. 5, where the right-slit is in the passing state in this case. Here, the constructive intra-slit dual-wave interference condition $4d = 7\lambda_0/2\sqrt{\kappa_1}$ has been met for the right slit. However, the left slit is neither in the passing state nor in the blocking state at $\lambda_0 = 1.176 \mu\text{m}$, which is seen in an intermediate state between these two with $4d = (7/2)\lambda_0/2\sqrt{\kappa_{-1}}$.

To get a complete picture about the intra-slit dual-wave interference at $\lambda_0 = 1.176 \mu\text{m}$, we show the slit-averaged ratio of $|H_y(x, z)|^2$ at $\lambda_0 = 1.176 \mu\text{m}$ in Fig. 6 as a function of d . Indeed, we find from this figure that there exists a set of minima for the right slit at $2d/\lambda_0 = 2/8, 4/8, 6/8$ and $8/8$ with $\sqrt{\kappa_1} = 2$, as well as a group of maxima at $2d/\lambda_0 = 1/8, 3/8, 5/8$ and $7/8$. We also notice here that dips, instead of maxima, still show up for the left slit at $2d/\lambda_0 = 2/8$ and $6/8$ with $\sqrt{\kappa_{-1}} = 1$ due to incomplete inter-slit dual-wave constructive interference as discussed in connection with Fig. 4. Interestingly, we also find very narrow peaks right above two of the four blocking states of the right slit, and these sharp peaks get stronger with increased slit depth. The occurrence of two extremely sharp peaks in this figure can be qualitatively attributed to the result of the Fabry-Pérot sole-wave interference between the entry and exit edges of the right slit with a finite value for the average reflection coefficient (or a large finesse). The peak positions from a constructive Fabry-Pérot interference coincidentally overlaps with two of the four slit blocking states. Although the slit widths in Figs. 5 and 6 are different, it will not change the peak and valley positions for the dominant lowest symmetric slit mode.

The current paper deals with a real metallic film by imposing the SIBC in Eqs. (1) and (2) for a finite metal conductivity. This facilitates the propagation of the SP polariton wave, which is excited at the middle slit, to two neighboring side slits. Consequently, for a PEC with $\eta_L = \eta_R = 0$ we expect the passing state of the left slit in Fig. 2 will become much

weaker, which can be clearly seen from the calculated transmitted near-field distribution in Fig. 7. In the case of a PEC, no SP polariton wave is excited on the backside of the metal film, and the reflection from the illuminated middle slit on the front-side of the film becomes very collimated in the near-field region. Moreover, the maximum intensity in Fig. 2 occurs farther from the film than it does in Fig. 7, and the angular distribution of the intensity of the transmitted field is broader in Fig. 2 than it is in Fig. 7. There exists a major difference in the coupling between slits on the interface of a PEC or a real metal. For the former, only radiative modes out of the metal plane can contribute, while both surface-plasmon and radiative modes will contribute to the latter.

Finally, we know from Fig. 5 that the left slit is in an intermediate state although the right slit is in a passing state at $\lambda_0 = 1.176 \mu\text{m}$. The ideal situation is that the left slit could be forced into a blocking state at this wavelength. This goal can be reached if the filled dielectric medium in the left slit can be tuned from $\sqrt{\kappa-1} = 1$ to $\sqrt{\kappa-1} = 4$, which has been simulated by the calculated transmitted near-field distribution displayed in Fig. 8.

4. Conclusions

In conclusion, motivated by the previous Green's function formalism^{12,15}, we have derived a scattering-wave theory to study the wavelength-dependent detection of surface-plasmon mediated light-beam splitting into two by a triple-slit structure perforated by a gold film and filled with different slit materials. This can be viewed as a new addition to the previously demonstrated longitudinal color-dependent light focusing using a finite groove array with various groove widths in a parabolic pattern. For a specifically chosen slit depth, filled slits dielectric material, and inter-slit distance in the deep sub-wavelength regime, we have found that only one of the two side observation slits is in a passing state for a particular wavelength, but the other blocked slit switches to a passing state at double that wavelength. In this sense, surface-plasmon mediated light-beam splitting becomes wavelength sensitive, and a single light-beam incidence with two wavelengths can be separated along the transverse direction parallel to the array. This provides us with a direct optical reading in the near-field region based on a non-spectroscopic technique.

Acknowledgments

We would like to thank the Air Force Office of Scientific Research (AFOSR) for its support. We would also like to thank helpful suggestions as well as a critical reading of the paper by Prof. A. A. Maradudin.

Appendix A

The overlap integrals initially introduced in Eqs. (13) and (14) are defined as follows:

$$\begin{aligned} Q_{sn}^j(\beta) &= \frac{1}{\ell_j} \int_{-\ell_j}^{\ell_j} dz \cos(\xi_{sn}^j z) \cos(\beta z) \\ &= \text{sinc}[(\beta - \xi_{sn}^j) \ell_j] + \text{sinc}[(\beta + \xi_{sn}^j) \ell_j] , \end{aligned} \quad (26)$$

$$\begin{aligned} Q_{an}^j(\beta) &= \frac{1}{\ell_j} \int_{-\ell_j}^{\ell_j} dz \sin(\xi_{an}^j z) \sin(\beta z) \\ &= \text{sinc}[(\beta - \xi_{an}^j) \ell_j] - \text{sinc}[(\beta + \xi_{an}^j) \ell_j] , \end{aligned} \quad (27)$$

and $\text{sinc}(x) \equiv \sin x/x$.

Appendix B

The coupling matrices initially introduced in Eqs. (13), (14), (15) and (16) are defined as

$$\begin{aligned} P_s(\beta, \beta') &= \int_{-\infty}^{-|z_{-N} - \ell_{-N}|} \cos(\beta' z) \cos(\beta z) dz + \int_{z_N + \ell_N}^{\infty} \cos(\beta' z) \cos(\beta z) dz \\ &= \pi [\delta(\beta - \beta') + \delta(\beta + \beta')] \\ &\quad - \frac{|z_{-N} - \ell_{-N}|}{2} \{ \text{sinc}[(\beta + \beta')|z_{-N} - \ell_{-N}|] + \text{sinc}[(\beta - \beta')|z_{-N} - \ell_{-N}|] \} \\ &\quad - \frac{z_N + \ell_N}{2} \{ \text{sinc}[(\beta + \beta')(z_N + \ell_N)] + \text{sinc}[(\beta - \beta')(z_N + \ell_N)] \} , \end{aligned} \quad (28)$$

$$\begin{aligned}
P_a(\beta, \beta') &= \int_{-\infty}^{-|z_{-N}-\ell_{-N}|} \sin(\beta' z) \sin(\beta z) dz + \int_{z_N+\ell_N}^{\infty} \sin(\beta' z) \sin(\beta z) dz \\
&= \pi [\delta(\beta - \beta') - \delta(\beta + \beta')] \\
&+ \frac{|z_{-N}-\ell_{-N}|}{2} \{ \text{sinc}[(\beta + \beta')|z_{-N}-\ell_{-N}|] - \text{sinc}[(\beta - \beta')|z_{-N}-\ell_{-N}|] \} \\
&+ \frac{z_N+\ell_N}{2} \{ \text{sinc}[(\beta + \beta')(z_N+\ell_N)] - \text{sinc}[(\beta - \beta')(z_N+\ell_N)] \} , \tag{29}
\end{aligned}$$

$$\begin{aligned}
P_c(\beta, \beta') &= \int_{-\infty}^{-|z_{-N}-\ell_{-N}|} \sin(\beta' z) \cos(\beta z) dz + \int_{z_N+\ell_N}^{\infty} \sin(\beta' z) \cos(\beta z) dz \\
&- \frac{1}{2} \left\{ \frac{\cos[(\beta + \beta')|z_{-N}-\ell_{-N}|]}{\beta + \beta'} - \frac{\cos[(\beta - \beta')|z_{-N}-\ell_{-N}|]}{\beta - \beta'} \right\} \\
&+ \frac{1}{2} \left\{ \frac{\cos[(\beta + \beta')(z_N+\ell_N)]}{\beta + \beta'} - \frac{\cos[(\beta - \beta')(z_N+\ell_N)]}{\beta - \beta'} \right\} , \tag{30}
\end{aligned}$$

$$\begin{aligned}
W_s(\beta, \beta') &= \sum_{j=-N}^{N-1} \int_{z_j+\ell_j}^{z_{j+1}-\ell_{j+1}} \cos(\beta' z) \cos(\beta z) dz \\
&= \frac{1}{2} \sum_{j=-N}^{N-1} \{ (z_{j+1} - \ell_{j+1}) (\text{sinc}[(\beta' - \beta)(z_{j+1} - \ell_{j+1})] \\
&+ \text{sinc}[(\beta' + \beta)(z_{j+1} - \ell_{j+1})]) \\
&- (z_j + \ell_j) (\text{sinc}[(\beta' + \beta)(z_j + \ell_j)] + \text{sinc}[(\beta' - \beta)(z_j + \ell_j)]) \} , \tag{31}
\end{aligned}$$

$$\begin{aligned}
W_a(\beta, \beta') &= \sum_{j=-N}^{N-1} \int_{z_j+\ell_j}^{z_{j+1}-\ell_{j+1}} \sin(\beta' z) \sin(\beta z) dz \\
&= \frac{1}{2} \sum_{j=-N}^{N-1} \{ (z_{j+1} - \ell_{j+1}) (\text{sinc}[(\beta' - \beta)(z_{j+1} - \ell_{j+1})] \\
&- \text{sinc}[(\beta' + \beta)(z_{j+1} - \ell_{j+1})]) \\
&+ (z_j + \ell_j) (\text{sinc}[(\beta' + \beta)(z_j + \ell_j)] - \text{sinc}[(\beta' - \beta)(z_j + \ell_j)]) \} , \tag{32}
\end{aligned}$$

$$\begin{aligned}
W_c(\beta, \beta') &= \sum_{j=-N}^{N-1} \int_{z_j+\ell_j}^{z_{j+1}-\ell_{j+1}} \sin(\beta' z) \cos(\beta z) dz \\
&= \frac{1}{2} \sum_{j=-N}^{N-1} \left\{ \frac{\cos[(\beta' - \beta)(z_j + \ell_j)]}{\beta' - \beta} + \frac{\cos[(\beta' + \beta)(z_j + \ell_j)]}{\beta' + \beta} \right. \\
&\quad \left. - \frac{\cos[(\beta' - \beta)(z_{j+1} - \ell_{j+1})]}{\beta' - \beta} - \frac{\cos[(\beta' + \beta)(z_{j+1} - \ell_{j+1})]}{\beta' + \beta} \right\} . \tag{33}
\end{aligned}$$

Appendix C

We have introduced in Eq. (21) the following amplitudes

$$\begin{aligned}
Y_{jn}^{(1)} &= \frac{\sigma_{sn}^j \epsilon_L}{\chi_n \kappa_j} \int_0^\infty \frac{d\beta}{k_1(\beta)} Q_{sn}^j(\beta) \\
&\times \{ [G_s(\beta) - A_s(\beta)] \cos(\beta z_j) + i [G_a(\beta) - A_a(\beta)] \sin(\beta z_j) \} , \tag{34}
\end{aligned}$$

$$Y_{jn}^{(2)} = \frac{\sigma_{sn}^j \epsilon_R}{\chi_n \kappa_j} \int_0^\infty \frac{d\beta}{k_2(\beta)} Q_{sn}^j(\beta) [B_s(\beta) \cos(\beta z_j) + i B_a(\beta) \sin(\beta z_j)] , \tag{35}$$

$$\begin{aligned}
X_{jn}^{(1)} &= \frac{\sigma_{an}^j \epsilon_L}{\chi_n \kappa_j} \int_0^\infty \frac{d\beta}{k_1(\beta)} Q_{an}^j(\beta) \\
&\times \{ [G_a(\beta) - A_a(\beta)] \cos(\beta z_j) + i [G_s(\beta) - A_s(\beta)] \sin(\beta z_j) \} , \tag{36}
\end{aligned}$$

$$X_{jn}^{(2)} = \frac{\sigma_{an}^j \epsilon_R}{\chi_n \kappa_j} \int_0^\infty \frac{d\beta}{k_2(\beta)} Q_{an}^j(\beta) [B_a(\beta) \cos(\beta z_j) + i B_s(\beta) \sin(\beta z_j)] . \tag{37}$$

Appendix D

In Eqs. (22) through (25) we have introduced the following matrices

$$\begin{aligned}
& \begin{bmatrix} T_s^{(1)}(\beta, \beta') \\ T_s^{(2)}(\beta, \beta') \\ T_s^{(3)}(\beta, \beta') \\ T_s^{(4)}(\beta, \beta') \end{bmatrix} = \frac{1}{i\pi} \sum_{n,j} \left[\frac{\sigma_{sn}^j \ell_j}{\chi_n \kappa_j \sin(2\sigma_{sn}^j d)} \right] Q_{sn}^j(\beta) Q_{sn}^j(\beta') \\
& \times \begin{bmatrix} \epsilon_R \cos(\beta z_j) \cos(\beta' z_j) \\ \epsilon_R \cos(\beta z_j) \sin(\beta' z_j) \\ \epsilon_L \cos(2\sigma_{sn}^j d) \cos(\beta z_j) \cos(\beta' z_j) \\ \epsilon_L \cos(2\sigma_{sn}^j d) \cos(\beta z_j) \sin(\beta' z_j) \end{bmatrix}, \tag{38}
\end{aligned}$$

$$\begin{aligned}
& \begin{bmatrix} R_s^{(1)}(\beta, \beta') \\ R_s^{(2)}(\beta, \beta') \\ R_s^{(3)}(\beta, \beta') \\ R_s^{(4)}(\beta, \beta') \end{bmatrix} = \frac{1}{i\pi} \sum_{n,j} \left[\frac{\sigma_{an}^j \ell_j}{\chi_n \kappa_j \sin(2\sigma_{an}^j d)} \right] Q_{an}^j(\beta) Q_{an}^j(\beta') \\
& \times \begin{bmatrix} \epsilon_R \sin(\beta z_j) \cos(\beta' z_j) \\ \epsilon_R \sin(\beta z_j) \sin(\beta' z_j) \\ \epsilon_L \cos(2\sigma_{an}^j d) \sin(\beta z_j) \cos(\beta' z_j) \\ \epsilon_L \cos(2\sigma_{an}^j d) \sin(\beta z_j) \sin(\beta' z_j) \end{bmatrix}, \tag{39}
\end{aligned}$$

$$\begin{aligned}
& \begin{bmatrix} T_a^{(1)}(\beta, \beta') \\ T_a^{(2)}(\beta, \beta') \\ T_a^{(3)}(\beta, \beta') \\ T_a^{(4)}(\beta, \beta') \end{bmatrix} = \frac{1}{i\pi} \sum_{n,j} \left[\frac{\sigma_{sn}^j \ell_j}{\chi_n \kappa_j \sin(2\sigma_{sn}^j d)} \right] Q_{sn}^j(\beta) Q_{sn}^j(\beta') \\
& \times \begin{bmatrix} \epsilon_R \sin(\beta z_j) \cos(\beta' z_j) \\ \epsilon_R \sin(\beta z_j) \sin(\beta' z_j) \\ \epsilon_L \cos(2\sigma_{sn}^j d) \sin(\beta z_j) \cos(\beta' z_j) \\ \epsilon_L \cos(2\sigma_{sn}^j d) \sin(\beta z_j) \sin(\beta' z_j) \end{bmatrix}, \tag{40}
\end{aligned}$$

$$\begin{aligned}
& \begin{bmatrix} R_a^{(1)}(\beta, \beta') \\ R_a^{(2)}(\beta, \beta') \\ R_a^{(3)}(\beta, \beta') \\ R_a^{(4)}(\beta, \beta') \end{bmatrix} = \frac{1}{i\pi} \sum_{n,j} \left[\frac{\sigma_{an}^j \ell_j}{\chi_n \kappa_j \sin(2\sigma_{an}^j d)} \right] Q_{an}^j(\beta) Q_{an}^j(\beta')
\end{aligned}$$

$$\times \begin{bmatrix} \epsilon_R \cos(\beta z_j) \cos(\beta' z_j) \\ \epsilon_R \cos(\beta z_j) \sin(\beta' z_j) \\ \epsilon_L \cos(2\sigma_{an}^j d) \cos(\beta z_j) \cos(\beta' z_j) \\ \epsilon_L \cos(2\sigma_{an}^j d) \cos(\beta z_j) \sin(\beta' z_j) \end{bmatrix}, \quad (41)$$

$$\begin{bmatrix} N_s^{(1)}(\beta, \beta') \\ N_s^{(2)}(\beta, \beta') \\ N_s^{(3)}(\beta, \beta') \\ N_s^{(4)}(\beta, \beta') \end{bmatrix} = \frac{1}{i\pi} \sum_{n,j} \left[\frac{\sigma_{sn}^j \ell_j}{\chi_n \kappa_j \sin(2\sigma_{sn}^j d)} \right] Q_{sn}^j(\beta) Q_{sn}^j(\beta') \\ \times \begin{bmatrix} \epsilon_R \cos(2\sigma_{sn}^j d) \cos(\beta z_j) \cos(\beta' z_j) \\ \epsilon_R \cos(2\sigma_{sn}^j d) \cos(\beta z_j) \sin(\beta' z_j) \\ \epsilon_L \cos(\beta z_j) \cos(\beta' z_j) \\ \epsilon_L \cos(\beta z_j) \sin(\beta' z_j) \end{bmatrix}, \quad (42)$$

$$\begin{bmatrix} M_s^{(1)}(\beta, \beta') \\ M_s^{(2)}(\beta, \beta') \\ M_s^{(3)}(\beta, \beta') \\ M_s^{(4)}(\beta, \beta') \end{bmatrix} = \frac{1}{i\pi} \sum_{n,j} \left[\frac{\sigma_{an}^j \ell_j}{\chi_n \kappa_j \sin(2\sigma_{an}^j d)} \right] Q_{an}^j(\beta) Q_{an}^j(\beta') \\ \times \begin{bmatrix} \epsilon_R \cos(2\sigma_{an}^j d) \sin(\beta z_j) \cos(\beta' z_j) \\ \epsilon_R \cos(2\sigma_{an}^j d) \sin(\beta z_j) \sin(\beta' z_j) \\ \epsilon_L \sin(\beta z_j) \cos(\beta' z_j) \\ \epsilon_L \sin(\beta z_j) \sin(\beta' z_j) \end{bmatrix}, \quad (43)$$

$$\begin{bmatrix} N_a^{(1)}(\beta, \beta') \\ N_a^{(2)}(\beta, \beta') \\ N_a^{(3)}(\beta, \beta') \\ N_a^{(4)}(\beta, \beta') \end{bmatrix} = \frac{1}{i\pi} \sum_{n,j} \left[\frac{\sigma_{sn}^j \ell_j}{\chi_n \kappa_j \sin(2\sigma_{sn}^j d)} \right] Q_{sn}^j(\beta) Q_{sn}^j(\beta') \\ \times \begin{bmatrix} \epsilon_R \cos(2\sigma_{sn}^j d) \sin(\beta z_j) \cos(\beta' z_j) \\ \epsilon_R \cos(2\sigma_{sn}^j d) \sin(\beta z_j) \sin(\beta' z_j) \\ \epsilon_L \sin(\beta z_j) \cos(\beta' z_j) \\ \epsilon_L \sin(\beta z_j) \sin(\beta' z_j) \end{bmatrix}, \quad (44)$$

$$\begin{aligned}
& \begin{bmatrix} M_a^{(1)}(\beta, \beta') \\ M_a^{(2)}(\beta, \beta') \\ M_a^{(3)}(\beta, \beta') \\ M_a^{(4)}(\beta, \beta') \end{bmatrix} = \frac{1}{i\pi} \sum_{n,j} \left[\frac{\sigma_{an}^j \ell_j}{\chi_n \kappa_j \sin(2\sigma_{an}^j d)} \right] Q_{an}^j(\beta) Q_{an}^j(\beta') \\
& \times \begin{bmatrix} \epsilon_R \cos(2\sigma_{an}^j d) \cos(\beta z_j) \cos(\beta' z_j) \\ \epsilon_R \cos(2\sigma_{an}^j d) \cos(\beta z_j) \sin(\beta' z_j) \\ \epsilon_L \cos(\beta z_j) \cos(\beta' z_j) \\ \epsilon_L \cos(\beta z_j) \sin(\beta' z_j) \end{bmatrix}. \tag{45}
\end{aligned}$$

References

1. H. Raether, *Surface Plasmons on Smooth and Rough Surfaces and on Gratings*, (Springer-Verlag, Berlin, 1988).
2. G. Gumbs and D. H. Huang, *Properties of Interacting Low-Dimensional Systems* (Wiley-VCH Verlag GmbH & Co. KGaA, Weinheim, Germany, 2011), Chaps. 4 and 5.
3. F. J. Garcia-Vidal, L. Martin-Moreno, T. W. Ebbesen, and L. Kuipers, “Light passing through subwavelength apertures,” *Rev. Mod. Phys.* **82**, 729-787 (2010) [and references therein].
4. T. W. Ebbesen, H. J. Lezec, H. F. Ghaemi, T. Thio and P. A. Wolff, “Extraordinary optical transmission through sub-wavelength hole arrays,” *Nature* **391**, 667-669 (1998).
5. H. F. Ghaemi, T. Thio, D. E. Grupp, T. W. Ebbesen and H. J. Lezec, “Surface plasmons enhance optical transmission through subwavelength holes,” *Phys. Rev. B* **58**, 6779-6782 (1998).
6. T. Thio, H. F. Ghaemi, H. J. Lezec, P. A. Wolff and T. W. Ebbesen, “Surface-plasmon-enhanced transmission through hole arrays in Cr films,” *J. Opt. Soc. Am. B* **16**, 1743-1748 (1999).
7. J. C.-C. Chang, Z.-P. Yang, D. H. Huang, D. A. Cardimona and S.-Y. Lin, “Strong light concentration at the subwavelength scale by a metallic hole-array structure,” *Opt.* **34**, 106-108 (2009).
8. J. C.-C. Chang, Y. D. Sharma, Y.-S. Kim, J. A. Bur, R. V. Shenoi, S. Krishna, D. H. Huang, and S.-Y. Lin, “A surface plasmon enhanced infrared photodetector based on InAs quantum dots,” *Nano Lett.* **10**, 1704-1709 (2010).
9. A. A. Maradudin, ed., *Light Scattering and Nanoscale Surface Roughness*, (Springer Science+Business Media, LLC., New York, 2007).
10. A. V. Zayats, I. I. Smolyaninov, and A. A. Maradudin, “Nano-optics of surface plasmon polaritons,” *Phys. Rep.* **408**, 131-314 (2005) [and references therein].
11. F. de Leon-Perez, G. Brucoli, F. J. Garcia-Vidal, and L. Martin-Moreno, “Theory on the scattering of light and surface plasmon polaritons by arrays of holes and dimples in a metal film,” *New J. Phys.* **10**, 105017 (2008).
12. B. Baumeier, T. A. Leskova, and A. A. Maradudin, “Transmission of light through a thin metal film with periodically and randomly corrugated surfaces,” *J. Opt. A, Pure*

- Appl. Opt. **8**, S191-S207 (2006).
13. E. Laux, C. Genet, T. Skauli, and T. W. Ebbesen, "Plasmonic photon sorters for spectral and polarimetric imaging," Nat. Photon. **2**, 161-164 (2008).
 14. L. D. Wellems, D. H. Huang, T. A. Leskova and A. A. Maradudin, "Nanogroove array on thin metallic film as planar lens with tunable focusing," Phys. Lett. A **376**, 216 (2012).
 15. L. D. Wellems, D. H. Huang, T. A. Leskova, and A. A. Maradudin, "Optical spectrum and electromagnetic-field distribution at double-groove metallic surface gratings," J. Appl. Phys. **106**, 053705 (2009).
 16. F. López-Tejeira, F. J. Garcia-Vidal, and L. Martin-Moreno, "Scattering of surface plasmons by one-dimensional periodic nanoindented surfaces," Phys. Rev. B **72**, 161405 (2005).
 17. T. A. Leskova, A. A. Maradudin, and I. Novikov, "Impedance Boundary Conditions for a Metal Film with a Rough Surface," Appl. Opt. **38**, 1197-1212 (1999).
 18. A. A. Maradudin and A. Sentenac, "The impedance boundary condition for a periodically corrugated metal surface," Solid State Comm. **84**, 159-163 (1992).
 19. H. Lochbihler and R. Depine, "Highly conducting wire gratings in the resonance region," Appl. Opt. **32**, 3459-3465 (1993).
 20. D. Crouse, "Numerical modeling and electromagnetic resonant modes in complex grating structures and optoelectronic device applications," IEEE Trans. Electr. Devices, **52**, 2365-2373 (2005).
 21. P. B. Johnson and R. W. Christy, "Optical Constants of the Noble Metals," Phys. Rev. B **6**, 4370-4379 (1972).
 22. L. D. Wellems and D. H. Huang, "Near-field light focusing by a slit array in a planar metal film with nonuniform slit dielectric material," Am. J. Phys. **80**, 122-132 (2012).
 23. T. López-Rios, D. Mendoza, F. J. Garca-Vidal, J. Sánchez-Dehesa and B. Pannetier, "Surface Shape Resonances in Lamellar Metallic Gratings," Phys. Rev. Lett. **81**, 665-668 (1998).
 24. F. J. Garcia-Vidal, J. Sánchez-Dehesa, A. Dechelette, E. Bustarret, T. López-Rios, T. Fournier and B. Pannetier, "Localized Surface Plasmons in Lamellar Metallic Gratings," J. Lightwave Tech. **17**, 2191-2195 (1999).
 25. V. M. Serdyuk, "Diffraction of a plane electromagnetic wave by a slot in a conducting

- screen of arbitrary thickness,” *Techn. Phys.* **50**, 1076-1083 (2005); “Exact solutions for electromagnetic wave diffraction by a slot and strip,” *Int. J. Electron. Commun. (AEO)* **65**, 182-189 (2011).
26. D. H. Huang, G. Gumbs, P. M. Alsing, and D. A. Cardimona, “Nonlocal mode mixing and surface-plasmon-polariton-mediated enhancement of diffracted terahertz fields by a conductive grating,” *Phys. Rev. B* **77**, 165404 (2008).
27. D. H. Huang, G. Gumbs and S.-Y. Lin, “Self-consistent theory for near-field distribution and spectrum with quantum wires and a conductive grating in terahertz regime,” *J. Appl. Phys.* **105**, 093715 (2009).
28. A. Jeffrey and D. Zwillinger, *Table of Integrals, Series, and Products*, 7th Edition, (Academic Press, Singapore, 2007).

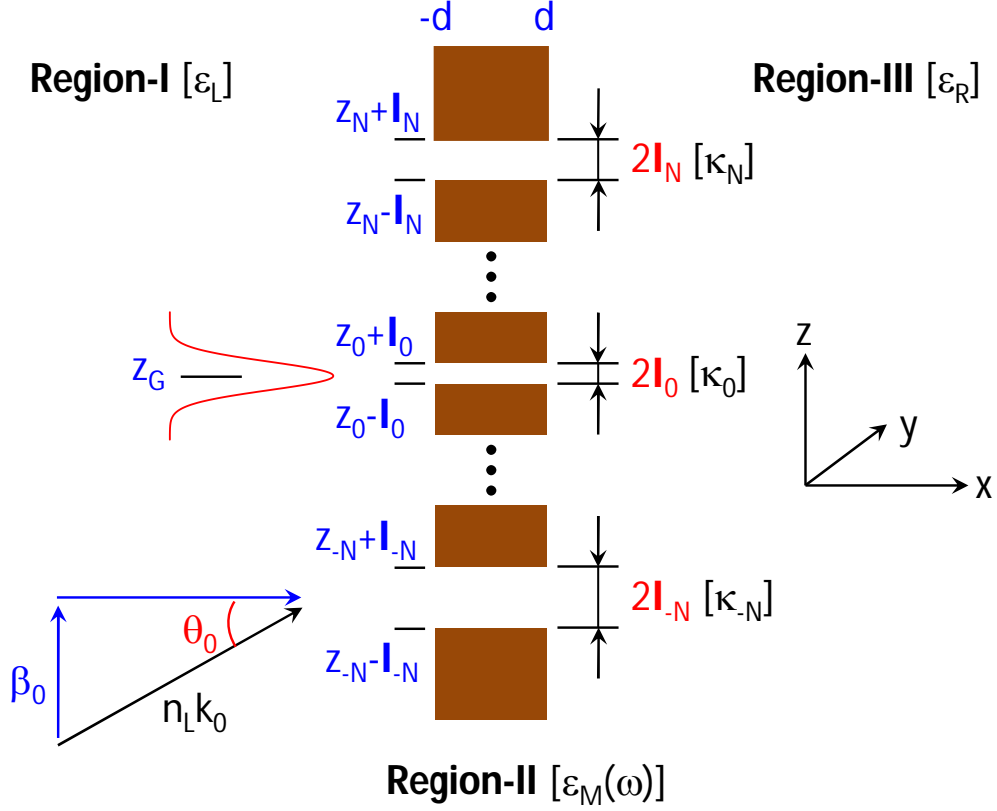


Fig. 1. (Color online) Illustration for a z direction slit array (brown) which extends in the y direction, where z_j and $2\ell_j$ are the center position and the width of the j th slit with $j = 0, \pm 1, \dots, \pm N$. The regions at the left- and right-hand side of the slits are denoted as Region I and Region III, respectively, with real dielectric constants ϵ_L and ϵ_R . The region for the slit array is denoted as Region II, and slits are filled with medium having a dielectric constant κ_j (real or complex) for $j = 0, \pm 1, \dots, \pm N$. The depth of slits in the x direction is $2d$, and $\epsilon_M(\omega)$ represents the dielectric function of the metal film containing slits. A Gaussian beam is incident on the slit array from the left side with an incident angle θ_0 and at a center position $z = z_G$. The incident wave number is $\sqrt{\epsilon_L} k_0$ and β_0 is the incident wave vector along the z direction.

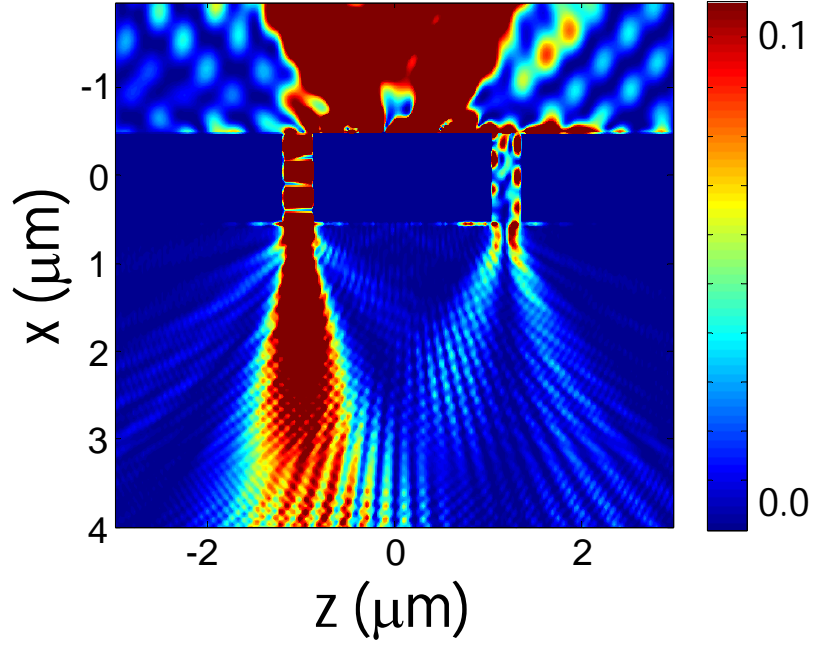


Fig. 2. (Color online) Contour plot of $|H_y(x, z)|^2$ for p -polarization normal incidence (from upper surface) with $\theta_0 = 0^\circ$, where $n_L = 1$ and $n_R = 4.5$. In our calculations, we set the parameters as follows: $\ell_{-1} = \ell_0 = \ell_1 = \zeta/4$, $\sqrt{\kappa_{-1}} = 1$, $\sqrt{\kappa_0} = 1 + 30i$, $\sqrt{\kappa_1} = 2$, $z_{-1}/\zeta = -1.75$, $z_0 = z_G = 0$, $z_1/\zeta = 2$, $d = (7/8)\zeta$, $g = 6\ell_0$, and $\lambda_0 = \zeta$, where $\zeta = 0.588 \mu\text{m}$.

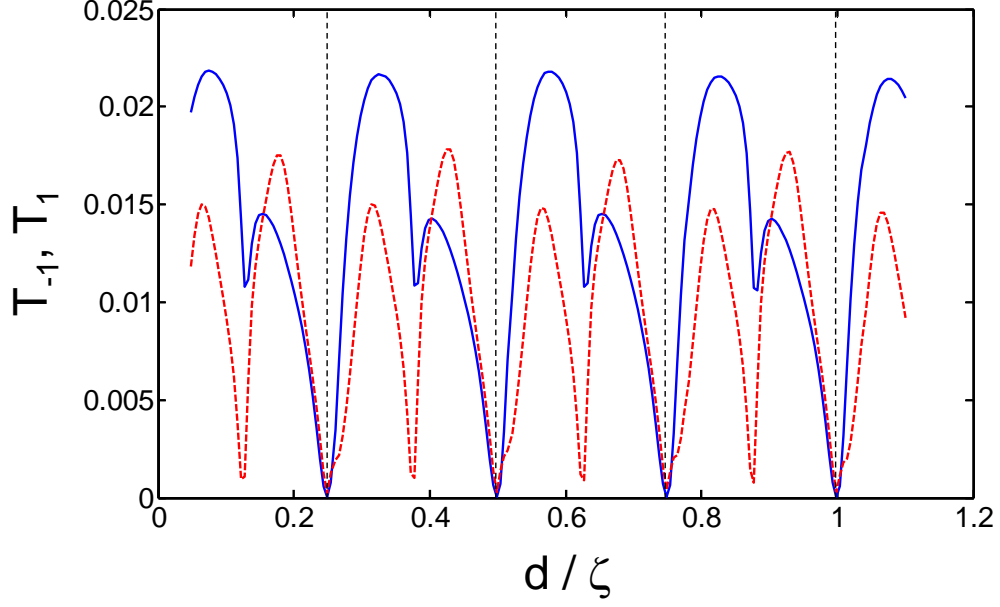


Fig. 3. (Color online) Plot for calculated $T_j = (1/2\ell_j) \int_{-\ell_j}^{\ell_j} dz |H_y(d + \delta, z - z_j)|^2$ for $j = -1$ (blue solid curve) and 1 (red dashed curve) as a function of slit depth d/ζ for p -polarization normal incidence as in Fig. 2, where $n_L = 1$, $n_R = 4.5$, $\delta = \zeta/2$ and the vertical black dashed lines indicate the positions determined by $d/\zeta = 2/8, 4/8, 6/8, 8/8$. In our calculations, we set the parameters as follows: $\ell_{-1} = \ell_0 = \ell_1 = \zeta/6$, $\sqrt{\kappa_{-1}} = 1$, $\sqrt{\kappa_0} = 1 + 30i$, $\sqrt{\kappa_1} = 2$, $z_{-1}/\zeta = -1.75$, $z_0 = z_G = 0$, $z_1/\zeta = 2$, $g = 6\ell_0$, and $\lambda_0 = \zeta$, where $\zeta = 0.588 \mu\text{m}$.

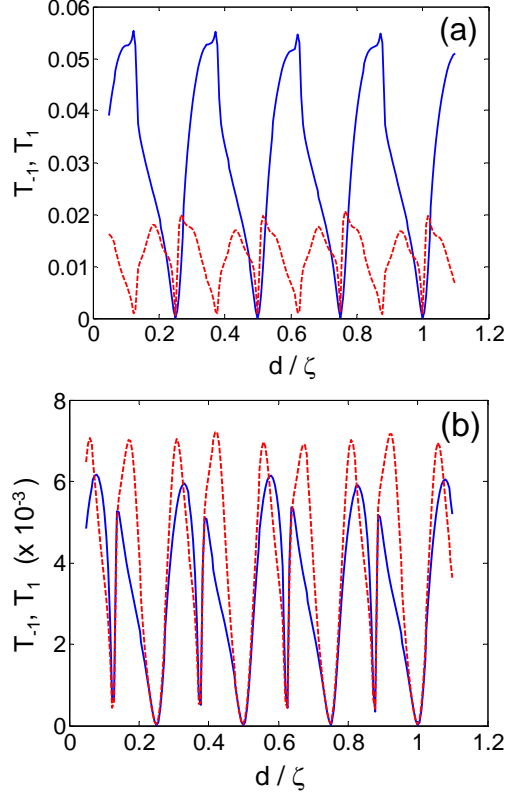


Fig. 4. (Color online) Plot for calculated $T_j = (1/2\ell_j) \int_{-\ell_j}^{\ell_j} dz |H_y(d + \delta, z - z_j)|^2$ for $j = -1$ (blue solid curve) and 1 (red dashed curve) as a function of slit depth d/ζ for p -polarization normal incidence as in Fig. 2, where $n_L = 1$, $n_R = 4.5$, $\delta = \zeta/2$. In our calculations, we set the parameters as follows: $\ell_{-1} = \ell_0 = \ell_1 = \zeta/6$, $\sqrt{\kappa_{-1}} = 1$, $\sqrt{\kappa_0} = 1 + 30i$, $\sqrt{\kappa_1} = 2$, $z_0 = z_G = 0$, $z_1/\zeta = 2$, $g = 6\ell_0$, and $\lambda_0 = \zeta$, where $\zeta = 0.588 \mu\text{m}$. Here, we chose $z_{-1}/\zeta = -1.5$ [in (a)] and $z_{-1}/\zeta = -2$ [in (b)], respectively.

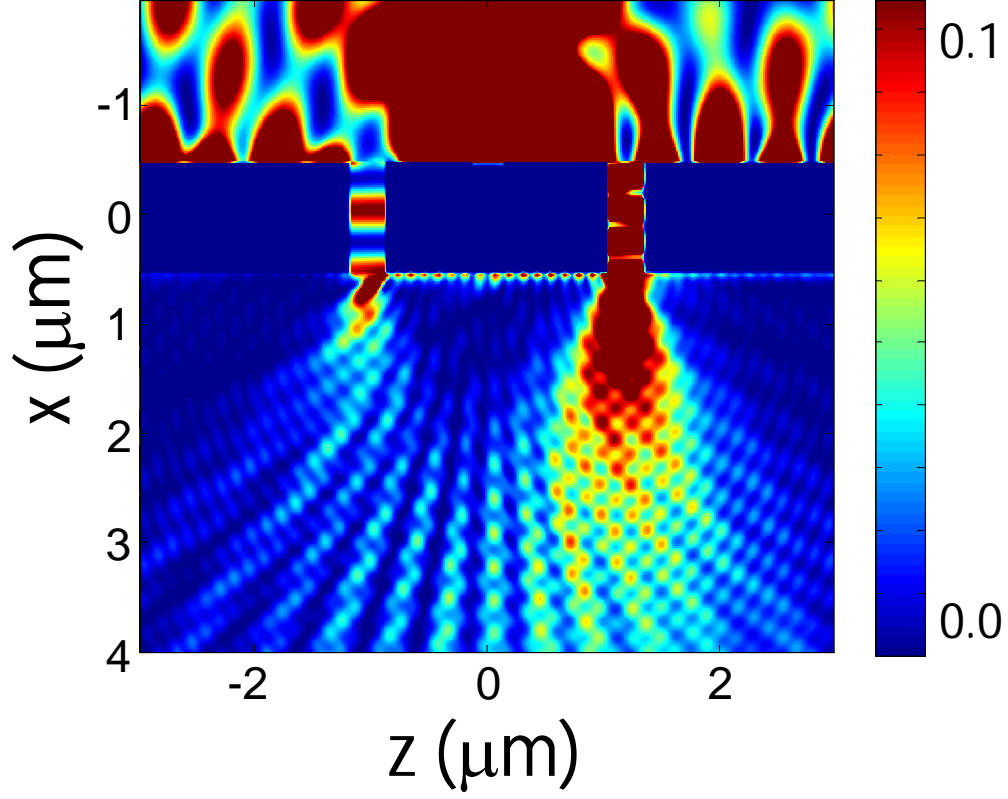


Fig. 5. (Color online) Contour plot of $|H_y(x, z)|^2$ for p -polarization normal incidence (from upper surface) with $\theta_0 = 0^\circ$, where $n_L = 1$ and $n_R = 4.5$. In our calculations, we set the parameters as follows: $\ell_{-1} = \ell_0 = \ell_1 = \zeta/4$, $\sqrt{\kappa_{-1}} = 1$, $\sqrt{\kappa_0} = 1 + 30i$, $\sqrt{\kappa_1} = 2$, $z_{-1}/\zeta = -1.75$, $z_0 = z_G = 0$, $z_1/\zeta = 2$, $d = (7/8)\zeta$, $g = 6\ell_0$, and $\lambda_0 = 2\zeta$, where $\zeta = 0.588 \mu\text{m}$.

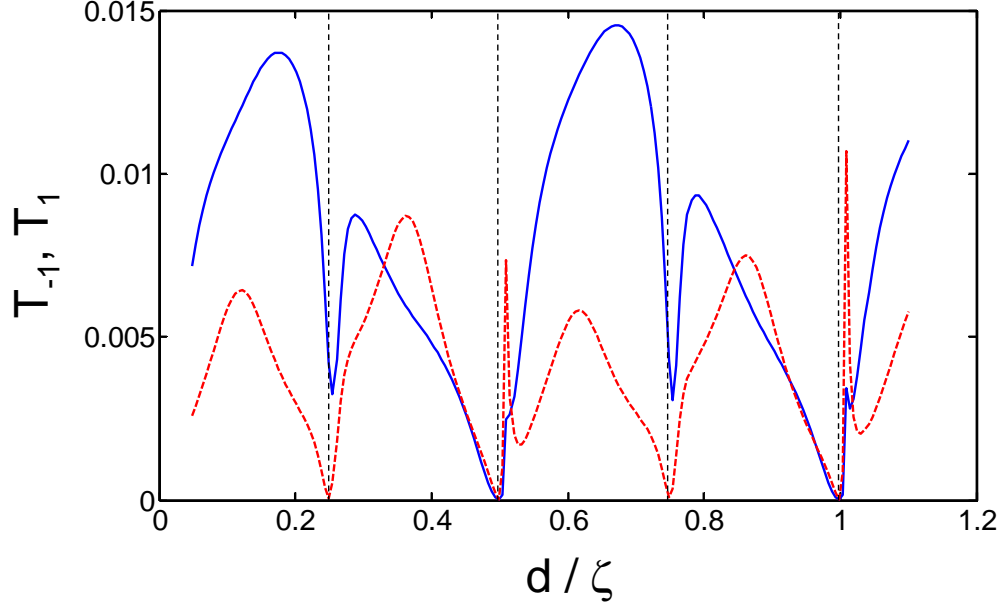


Fig. 6. (Color online) Plot for calculated $T_j = (1/2\ell_j) \int_{-\ell_j}^{\ell_j} dz |H_y(d + \delta, z - z_j)|^2$ for $j = -1$ (blue solid curve) and 1 (red dashed curve) as a function of slit depth d/ζ for p -polarization normal incidence as in Fig. 5, where $n_L = 1$, $n_R = 4.5$, $\delta = \zeta/2$ and the vertical black dashed lines indicate the positions determined by $d/\zeta = 2/8, 4/8, 6/8, 8/8..$ In our calculations, we set the parameters as follows: $\ell_{-1} = \ell_0 = \ell_1 = \zeta/6$, $\sqrt{\kappa_{-1}} = 1$, $\sqrt{\kappa_0} = 1 + 30i$, $\sqrt{\kappa_1} = 2$, $z_{-1}/\zeta = -1.75$, $z_0 = z_G = 0$, $z_1/\zeta = 2$, $g = 6\ell_0$, and $\lambda_0 = 2\zeta$, where $\zeta = 0.588 \mu\text{m}$.

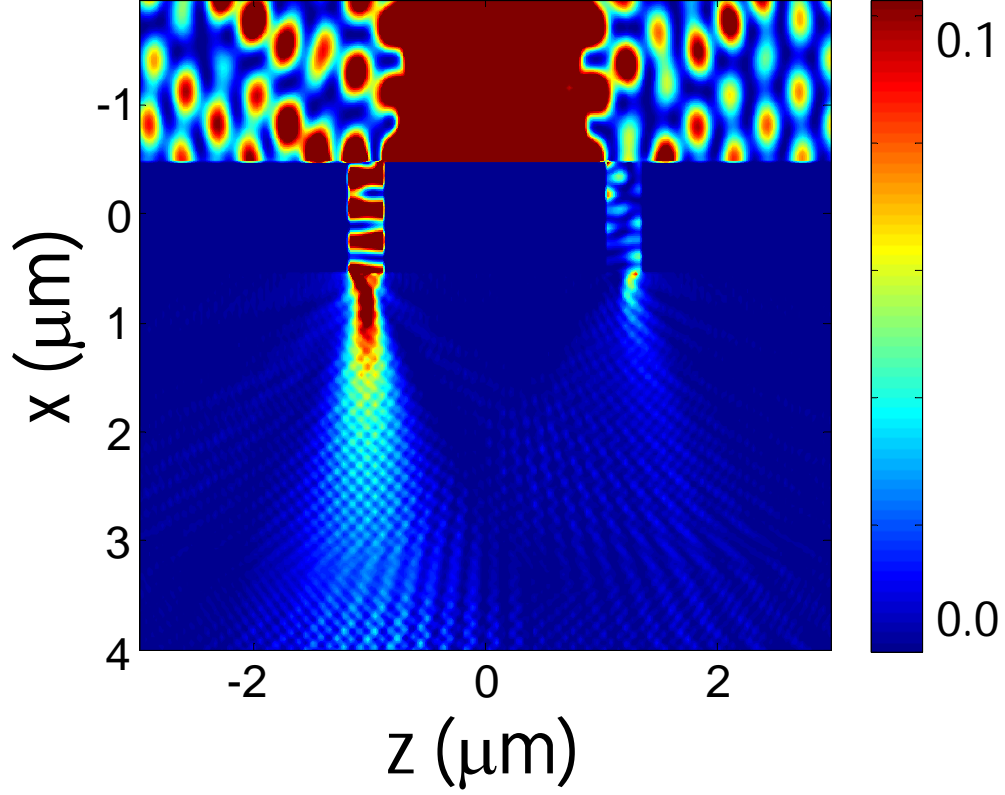


Fig. 7. (Color online) Contour plot of $|H_y(x, z)|^2$ for p -polarization normal incidence (from upper surface) with $\theta_0 = 0^\circ$, where $n_L = 1$ and $n_R = 4.5$. In our calculations, we set the parameters as follows: $\ell_{-1} = \ell_0 = \ell_1 = \zeta/4$, $\sqrt{\kappa_{-1}} = 1$, $\sqrt{\kappa_0} = 1 + 30i$, $\sqrt{\kappa_1} = 2$, $z_{-1}/\zeta = -1.75$, $z_0 = z_G = 0$, $z_1/\zeta = 2$, $d = (7/8)\zeta$, $g = 6\ell_0$, and $\lambda_0 = \zeta$, where $\zeta = 0.588 \mu\text{m}$. In this case, we set $\eta_L = \eta_R = 0$ for a perfect electric conductor.

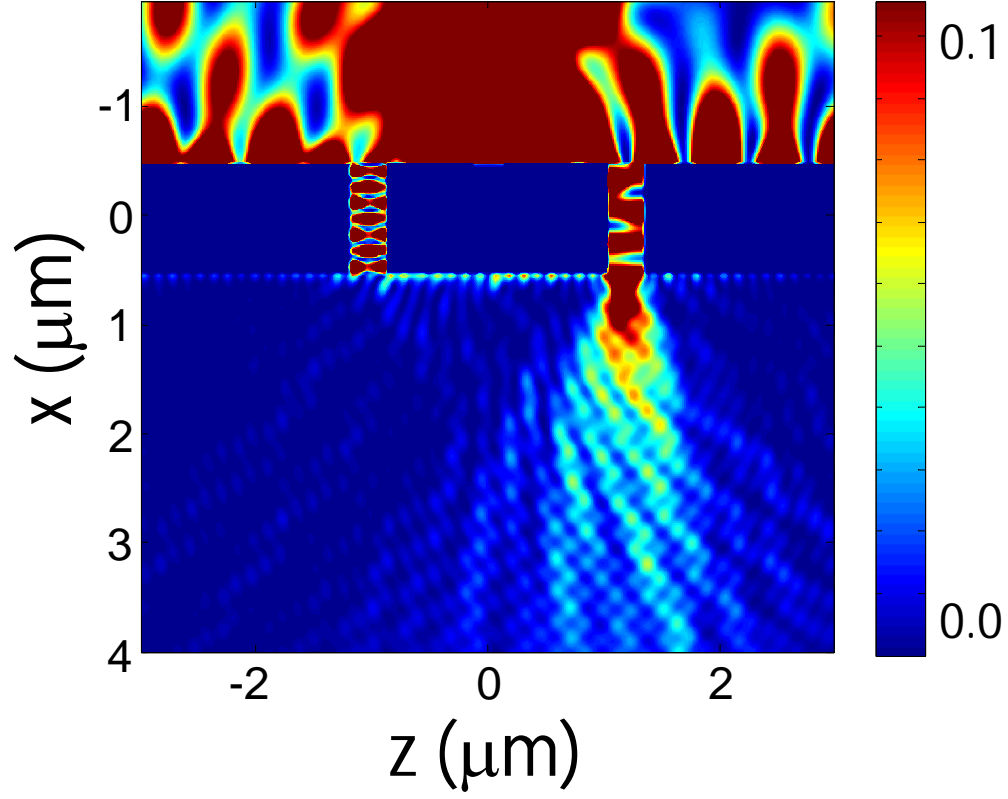


Fig. 8. (Color online) Contour plot of $|H_y(x, z)|^2$ for p -polarization normal incidence (from upper surface) with $\theta_0 = 0^\circ$, where $n_L = 1$ and $n_R = 4.5$. In our calculations, we set the parameters as follows: $\ell_{-1} = \ell_0 = \ell_1 = \zeta/4$, $\sqrt{\kappa_{-1}} = 4$, $\sqrt{\kappa_0} = 1 + 30i$, $\sqrt{\kappa_1} = 2$, $z_{-1}/\zeta = -1.75$, $z_0 = z_G = 0$, $z_1/\zeta = 2$, $d = (7/8)\zeta$, $g = 6\ell_0$, and $\lambda_0 = 2\zeta$, where $\zeta = 0.588 \mu\text{m}$.